Enhanced mitochondrial biogenesis promotes neuroprotection in human stem cell derived retinal ganglion cells of the central nervous system

Michelle Surma[1,7], Kavitha Anbarasu[1,2,7], Sayanta Dutta[1], Leonardo J. Olivera Perez[3], Kang-Chieh Huang[4], Jason S. Meyer[1,2,3,5] and Arupratan Das[1,2,5,6,*]

[1]Department of Ophthalmology, Eugene and Marilyn Glick Eye Institute, Indiana University, Indianapolis, IN 46202, USA; [2]Department of Medical and Molecular Genetics, Indiana University, Indianapolis, IN 46202, USA; [3]Indiana University School of Medicine, Indianapolis, IN 46202, USA; [4]Department of Biology, Indiana University Purdue University Indianapolis; [5]Stark Neurosciences Research Institute, Indiana University, Indianapolis, IN 46202, USA

[6]Lead Contact

[*]Correspondence: arupdas@iu.edu

[7]These authors contributed equally: Michelle Surma, Kavitha Anbarasu

Mitochondrial dysfunctions are widely afflicted in central nervous system (CNS) disorders with minimal understanding on how to improve mitochondrial homeostasis to promote neuroprotection. Here we used human stem cell differentiated retinal ganglion cells (hRGCs) of the CNS, which are highly sensitive towards mitochondrial dysfunctions due to their unique structure and function, to identify mechanisms for improving mitochondrial quality control (MQC). We found that hRGCs are efficient in maintaining mitochondrial homeostasis through rapid degradation and biogenesis of mitochondria under acute damage. Using a glaucomatous Optineurin mutant (E50K) stem cell lines, we saw that at basal level mutant hRGCs possess less mitochondrial mass and suffer mitochondrial swelling due to excess ATP production load. Activation of mitochondrial biogenesis through pharmacological inhibition of the Tank binding kinase 1 (TBK1) restored energy

homeostasis, mitigated mitochondrial swelling with neuroprotection against acute mitochondrial damage for glaucomatous *E50K* hRGCs, revealing a novel neuroprotection mechanism.

Introduction

Neurons require an increased supply of ATP compared to other cells in order to establish membrane potential for neurotransmission and synaptic activity[1]. Oxidative phosphorylation (OXPHOS) in mitochondria is the primary source of cellular ATP, thus mitochondrial dysfunction often associates with the neurodegenerative diseases such as mitochondrial optic neuropathies (MONs)[2], Parkinson's disease (PD)[3] and amyotrophic lateral sclerosis (ALS)[4]. Among central nervous system (CNS) neurons, retinal ganglion cells (RGCs) of the optic nerve require a steady source of ATP for their varying action potential (AP) firing frequency requirements and due to the existence of long partially unmyelinated axons. Axons of human RGCs remain unmyelinated after leaving the cell body in the retinal layer as they travel through the optic nerve head, until they reach the posterior end of lamina cribrosa[5]. APs through the unmyelinated axons propagate slowly and require more ATP[6]. Thus, human RGCs are the most sensitive towards mitochondrial dysfunctions. As such, inherited mutations in the complex I subunit of electron transport chain (ETC) cause Leber's hereditary optic neuropathy (LHON)[7], OPA1 mutations of the mitochondrial outer membrane protein required for mitochondrial fusion cause dominant optic atrophy (DOA)[8]; together these diseases are known as MONs[7].

Increased intraocular pressure (IOP) has been the major risk factor for glaucoma, however there are glaucoma patients with normal IOP, often referred to as normal-tension glaucoma (NTG)[9]. NTG patients are particularly challenging to treat as sufficient lowering of IOP is not always possible and a RGC protection strategy is yet to be discovered. Mutations in the mitochondrial homeostasis pathways are highly prevalent among NTG patients which includes the dominant Optineurin (*OPTN*^{E50K}) mutation. OPTN is a critical player for mitophagy and the E50K mutation is the most prevalent (~17%) among NTG patients[10,11]. Intriguingly, these inherited

52 mitochondrial mutations, though present in every cell of a patient's body, only cause death to
53 RGCs, leading to optic neuropathies. Thus, RGCs serve as a great neuronal model for
54 investigating mechanisms of improving mitochondrial homeostasis for developing
55 neuroprotection, which may be applicable to other CNS neurons. MQC involves biogenesis of
56 healthy mitochondria, fusion, fission, and degradation of damaged mitochondria (mitophagy)[8,9].
57 Thus, reduced mitochondrial homeostasis is expected in the E50K RGCs. However, to date we
58 have a very limited understanding on how to improve MQC to enhance RGC viability. RGCs
59 spontaneously degenerate at a slow rate during aging, however this degeneration is exacerbated
60 during optic neuropathies[5]. Thus, identification of mechanisms that will improve RGC survival
61 could provide therapy for optic neuropathies as well as for age related ganglion cell loss.

62 AMP-activated protein kinase (AMPK) is the master energy sensor in cells[12]. Decline in
63 energy homeostasis are associated with aging[13], obesity[14] and neurodegenerative conditions[15].
64 Thus, it is expected that a decline in mitochondrial homeostasis could lead to energy stress in
65 these disease conditions. Energy stress activates AMPK which activates proliferator-activated
66 receptor gamma co-activator 1α (PGC1α)[16], which is the master regulator of mitochondrial
67 biogenesis. Under normal conditions TBK1 phosphorylates the inhibitory site of AMPK[17] limiting
68 energy expenditure, which becomes counterproductive during aging and obesity. Conversely,
69 TBK1 inhibition has been found to increase energy expenditure, reduce obesity and insulin
70 resistance in mice[14]. It remains unexplored if targeting TBK1 could activate biogenesis of healthy
71 mitochondria leading to restoration of energy homeostasis and enhanced RGC survival under
72 disease conditions.

73 Here, we used a robust and well characterized human stem cell differentiated RGC
74 (hRGC) model to investigate if improving energy homeostasis through TBK1-AMPK pathway
75 could promote MQC and neuronal survival. It is critical to identify mechanisms for improving MQC
76 in human RGCs as mice RGCs are very different from human both anatomically and by genetic
77 makeup[18]. Differentiated hRGCs used here are well characterized and show the hallmark of

78 human RGCs, as characterized by their morphological features, gene-expression pattern, and
79 electrophysiological properties such as spontaneous generation of action potentials[19,20] and ability
80 to graft in the mice retina[21]. We have shown here that under acute mitochondrial damage hRGCs
81 activate the mitochondrial biogenesis pathway to maintain mitochondrial homeostasis.
82 Furthermore, we harnessed the biogenesis activation pathway by pharmacological inhibition of
83 TBK1 mediated activation of AMPK-PGC-1α biogenesis axis in hRGCs. Remarkably, activation
84 of mitochondrial biogenesis reduced metabolic burden in the glaucomatous E50K hRGCs leading
85 to recovery of mitochondrial swelling and pro-survival responses as an indication for
86 neuroprotection.
87
88 **Results**
89 **RGCs are highly efficient at degrading damaged mitochondria and producing**
90 **healthy mitochondria to maintain homeostasis under stress.** To investigate mitochondrial
91 homeostasis mechanisms in human RGCs we have used human stem cell differentiated RGCs
92 (hRGCs) following a robust method[19,22] where cells express RGC specific marker RBPMS and
93 neuronal marker Tubulin β3 (**Supplementary Fig. 1a, b**). Here, we have developed a "disease in
94 a dish" model for glaucoma using CRISPR engineered human embryonic stem cells with
95 glaucomatous *OPTN*^{E50K} mutation (H7-ESCs-E50K) (**Supplementary Fig. 1c**), patient derived
96 induced pluripotent stem cells with the E50K mutation (iPSCs-E50K)[23] and corresponding H7-
97 ESC and iPSC-E50K corrected (iPSC-E50Kcorr)[24] reporter lines for isogenic controls.[24] As RGCs
98 rely on a high ATP supply, it is likely that RGCs will be vulnerable towards mitochondrial damage
99 since they are the primary source for cellular ATP. We asked if hRGCs can maintain mitochondrial
100 homeostasis under acute damage. Carbonyl cyanide *m*-chlorophenylhydrazone (CCCP) has
101 been widely used in literature at 5-20 μM concentrations to induce mitochondrial damage[25,26]. This
102 has been shown, 10 μM of CCCP is effective in changing mitochondrial morphology within few

103 seconds in cultured cells[26]. We have previously performed a dose response and showed 10 μM
104 CCCP as minimum dose to have maximum mitochondrial degradation in hRGCs[22]. Here, we used
105 10 μM CCCP to cause acute mitochondrial damage for investigating how hRGCs restore
106 mitochondrial homeostasis under stress. We tested whether hRGCs maintain the same total
107 mitochondrial mass during CCCP damage by immunofluorescence against the mitochondria
108 specific protein Tom20 and by direct measurement of mitochondrial DNA copy number.
109 Interestingly, we found that the total mitochondrial mass fluctuates around DMSO control
110 condition during the course of CCCP treatment for both the WT and E50K hRGCs (**Fig. 1a-d).**
111 We further validated this observation by qPCR-based measurement of mitochondrial DNA copy
112 number relative to nuclear DNA and found WT hRGCs maintained mitochondrial mass similar to
113 the control condition while glaucomatous E50K hRGCs showed moderate reduction at the longer
114 CCCP treatment **(Fig. 1e, f).** These data suggest hRGCs possess stringent MQC mechanisms
115 for maintaining total mitochondrial mass even with acute damage. However, in these experiments
116 we measured total mitochondrial mass which cannot distinguish between the CCCP damaged
117 degrading mitochondria versus the newly synthesized population.

118 While hRGCs maintained total mitochondrial mass under acute CCCP damage, they
119 potentially have positive feedback where cells degrade damaged mitochondria, which activates
120 the biogenesis pathway to compensate the loss for maintaining energy homeostasis. Measuring
121 total mitochondrial mass in a cell will not resolve the newly synthesized versus the degrading
122 population. To directly measure mitochondrial degradation and biogenesis, we used a
123 mitochondria specific live cell dye MitoTracker Deep Red (MTDR) followed by flow cytometry-
124 based measurements, a protocol previously developed by us[22] but with modifications as explained
125 in Fig. 1g. The flow cytometry gating strategy is explained in **Supplementary Fig. 2**. MTDR
126 passively diffuses inside the mitochondria and retained based on active membrane potential, then
127 the dye covalently binds to the thiol groups of cysteine residue containing proteins[27]. Hence, once

128 labelled, any changes in the MTDR intensity should reflect the change in mitochondrial mass
129 independent of mitochondrial membrane polarity. For measuring CCCP induced mitochondrial
130 degradation, we first labelled existing mitochondria in hRGCs with MTDR followed by a wash step
131 and CCCP addition, and then flow cytometry-based measurements of mitochondrial mass in
132 single cells at different time points (**Fig. 1g**). In this study design, we measured MTDR labelled
133 mitochondrial mass in independent samples after different CCCP treatment timepoints. This
134 allowed us to track degradation of the labeled population while excluding any newly synthesized
135 mitochondria, as there was no dye in the media for new mitochondria to incorporate.
136 Quantification of MTDR intensity among the WT and E50K hRGCs showed a prompt (within 5
137 min) degradation of mitochondria upon CCCP treatment **(Fig. 1h).** Damaged mitochondria are
138 degraded by lysosomes via LC3B autophagic flux, a process known as mitophagy[28]. The hallmark
139 for activation of the mitophagy pathway is an increase in lipidated LC3B. Mitophagy complex
140 formation on mitochondria depends on the LC3B-I (non-lipidated, 16 kDa) to LC3B-II conversion
141 (lipidated, 14 kDa), which migrates faster during gel electrophoresis and enrichment of the second
142 band in western blot is a classic measurement of the induction of mitophagy[29]. We hypothesized
143 that induction of mitochondrial damage would lead to mitophagy by increasing LC3B lipidation.
144 Indeed, we observed rapid induction of mitophagy within 5 min of CCCP treatment as shown by
145 increased lipidated LC3B form in both WT (**Fig. 1i, j**) and E50K hRGCs (**Fig. 1k, l**). Of note, we
146 had previously shown lysosome dependent mitochondrial degradation in hRGCs is essential for
147 its viability[22]. This has also been shown that 10 μM of CCCP treatment for 5min induces
148 mitochondrial fragmentation for mitophagy in cultured HeLa cells and in mouse embryonic
149 fibroblasts (MEFs) further supporting our observations[26]. Since total mitochondrial mass
150 fluctuated close to the control condition under CCCP damage and above data identified
151 mitochondrial degradation under CCCP treatment by mitophagy, we asked if this mitochondrial
152 loss was compensated for by the biogenesis of new mitochondria.

153 For measuring mitochondrial biogenesis, we have modified the flow cytometry
154 experimental design to detect newly synthesized mitochondria. In this experimental design, we
155 first labelled mitochondria with MTDR, then treated cells with CCCP to cause mitochondrial
156 damage followed by a wash and media exchange containing MTDR but no CCCP, and then took
157 mitochondrial mass measurements at different timepoints (**Fig. 1g**). Here, after CCCP wash, the
158 newly synthesized mitochondria will incorporate MTDR, and we expect to see a gradual increase
159 in MTDR labelled mitochondrial mass over time. We found compared to DMSO control, 15min
160 after the CCCP wash there is a significant loss of labelled mitochondrial population, indicative of
161 degradation. Please note, mitochondria synthesized during the CCCP treatment are unlikely to
162 be detected by MTDR as CCCP depolarizes mitochondrial membrane potential and MTDR
163 retention requires intact membrane potential. However, after CCCP wash MTDR should bind to
164 the newly synthesized mitochondria, and indeed we observed hRGCs gradually increased
165 mitochondrial mass post CCCP wash and reached levels similar to the control condition after 24h
166 (**Fig. 1m).** These data suggest hRGCs possess highly efficient MQC mechanisms where they
167 efficiently degrade damaged mitochondria and produce healthy mitochondria to compensate the
168 loss, presumably maintaining their energy homeostasis.

169 To visualize the biogenesis and degradation events, we monitored mitochondrial turnover
170 using live cell JC1 dye which fluoresces green (monomers) when bound to damaged
171 (depolarized) and red (J aggregates) when bound to healthy (polarized) mitochondria[30]. We
172 expect, under biogenesis activation hRGCs will appear with more JC1 red mitochondria, and
173 under mitochondrial damage cells will have more JC1 green mitochondria. To visualize polarized
174 versus depolarized mitochondrial distribution at the basal level, we labelled mitochondria with the
175 JC1 dye and acquired live cell images, then added CCCP in the presence of the dye, to monitor
176 change in respective populations **(Fig. 2a)**. We observed at the basal level (before CCCP)
177 significant amounts of both JC1 labelled red and green mitochondria (**Fig. 2b**) indicating a
178 polarized and depolarized mitochondrial distribution. This observation is supported by cultured

179 healthy brain neurons that showed mitochondrial distribution with significant amounts of
180 depolarized (JC1 green) and polarized (JC1 red) membranes[31]. Interestingly, we observed an
181 increase in JC1 red intensity, but a more fragmented network and decrease in JC1 green
182 mitochondria for both the WT and E50K hRGCs upon CCCP damage (**Fig. 2b**) leading to
183 increased red-to-green ratio (**Fig. 2c**). This data is counterintuitive as we expected CCCP damage
184 will increase JC1 green mitochondria with a reduction of healthy mitochondria (red). However,
185 this observation could be supported if hRGCs efficiently clear CCCP damaged mitochondria and
186 simultaneously produce more to compensate the loss. Conversely, if we wash CCCP and allow
187 cells to recover, hRGCs should restore their depolarized to polarized mitochondrial distribution
188 like the basal level. To test this, we have performed a recovery experiment where we first treated
189 both WT and E50K hRGCs with CCCP or DMSO (control). Next, we washed CCCP and incubated
190 with JC1 media for recovery, then exchanged media without JC1 dye and acquired live cell
191 imaging to measure polarized to depolarized mitochondrial distribution (**Fig. 2d**). Indeed, we
192 observed WT hRGCs restored the mitochondrial distribution post CCCP wash similar to the
193 control (DMSO) condition (**Fig. 2e, f**). Although, at the basal level WT and E50K hRGCs possess
194 similar healthy to damaged mitochondrial ratio (**Fig. 2e, f**), after recovery from the CCCP damage,
195 E50K hRGCs showed reduced healthy mitochondrial mass compared to its control condition (**Fig.
196 2e, f**). This suggests that WT hRGCs possess a distribution of healthy and damaged mitochondria
197 at the basal level and are highly efficient in clearing acutely damaged mitochondria while
198 producing new to compensate the loss. This balance between the degradation and biogenesis
199 pathways helps hRGCs to regain mitochondrial homeostasis, however glaucomatous E50K
200 hRGCs struggle to restore homeostasis after acute damage.

201 **hRGCs activate the biogenesis signaling pathway under mitochondrial damage**.
202 Mitochondrial biogenesis has been shown to induce muscle growth after exercise[32] and synaptic
203 plasticity in neurons[33]. However, it is unknown if mitochondrial damage triggers activation of the
204 mitobiogenesis pathway in CNS neurons. AMP-activated protein kinase (AMPK) is a key regulator

205 of energy sensing and responds by increasing mitochondrial biogenesis[34]. AMPK is a
206 heterotrimeric protein activated by the phosphorylation of Thr172 in the AMPKα subunit[35] which
207 in turn activates PGC1α[14] at Ser571. PGC1α is the master regulator of mitochondrial biogenesis[36]
208 and is a transcriptional co-activator of nuclear respiratory factor 2 (NRF2) and NRF1 which
209 activate transcription factor A, mitochondrial (TFAM) for mitochondrial DNA (mtDNA) gene
210 expressions[37]. The biogenesis pathway can also be activated by the transcriptional co-activators
211 PGC1β and PGC1 related co-activator (PRC)[38]. We asked if mitochondrial damage leads to
212 activation of the AMPKα - PGC-1α axis for mitochondrial biogenesis in hRGCs. We induced
213 mitochondrial damage in hRGCs with CCCP and measured gene expressions of the biogenesis
214 pathway players such as PGC1α, PGC1β, NRF2, NRF1 and PRC. Indeed, we observed
215 significant increases of these gene expressions in both the WT and E50K hRGCs upon CCCP
216 mediated mitochondrial damage (**Fig. 3 a-d**). Next, we measured the biochemical activation of
217 the AMPKα and PGC1α proteins by immunoblotting against phosphorylated Thr172 and Ser571
218 for respective proteins under CCCP induced damage. We found at early CCCP exposure times
219 for both the WT and E50K hRGCs, a significant increase in the AMPKα activation which reduced
220 to the basal level during longer treatment (**Fig. 3e-g**). Furthermore, we observed a moderate
221 activation of the AMPKα effector PGC1α in the WT hRGCs but more significant increase in the
222 E50K hRGCs under CCCP treatments (**Fig. 3e, h, i**). These suggest mitochondrial damage
223 activates the energy sensor AMPKα in hRGCs which leads to the activation of the mito-biogenesis
224 master regulator PGC1α. The stronger PGC1α activation in E50K hRGCs suggests the need for
225 more healthy mitochondria, which is supported by our data showing E50K hRGCs struggle to
226 restore mitochondrial homeostasis after acute CCCP damage (**Fig. 2f**).

227 **TBK1 inhibition promotes mitochondrial biogenesis in hRGCs.** It has been reported
228 that TBK1 inhibits AMPKα in adipose tissue, and AMPK activation promotes mitochondrial
229 biogenesis through PGC-1α[14]. Hence, we asked if TBK1 inhibition will lead to the AMPK activation

230 which will promote mitochondrial biogenesis in hRGCs. BX795 drug is a potent TBK1 inhibitor[39]
231 that has been shown to resist the nerve fiber layer thinning of the glaucomatous E50K transgenic
232 mice retina[40]. We treated both WT and E50K hRGCs with BX795 and measured mitochondrial
233 mass by immunofluorescence against the mitochondria specific Tom20 protein. Surprisingly, we
234 observed at the basal level (DMSO control) E50K hRGCs possess significantly lower
235 mitochondrial mass compared to the WT (**Fig. 4a, b**). To validate that this observation is not due
236 to the indirect effect of DMSO vehicle control[41], we measured mitochondrial mass in untreated
237 WT and E50K hRGCs by Tom20 immunofluorescence. Our results further confirmed a
238 significantly lower mitochondrial mass in E50K hRGCs compared to the WT (**Supplementary**
239 **Fig. 3a, b)**. However, TBK1 inhibition by BX795 showed a robust increase in mitochondrial mass
240 at early and longer treatments for the WT and during longer treatments (18h, 24h) for E50K
241 hRGCs (**Fig. 4a, b**). We further confirmed the increase in mitochondrial mass by evaluating the
242 mitochondrial DNA copy number under BX795 treatment for both the WT and E50K hRGCs (**Fig.**
243 **4c, d**)[41]. To investigate whether BX795 increased mitochondrial mass by upregulating the
244 AMPKα-PGC1α axis, we measured the activation status of these proteins by immunoblotting
245 against respective activation site phosphorylation. Interestingly, we observed increased
246 activations of the AMPKα at longer BX795 treatment (24h) (**Fig. 4e, f**) and gradual activation of
247 PGC1α for WT hRGCs (**Fig. 4e, h**). However, such activation for AMPKα (**Fig. 4e, g**) and PGC1α
248 (**Fig. 4e, i**) were not observed for the E50K hRGCs under BX795 mediated TBK1 inhibition. Apart
249 from the AMPKα-PGC-1α axis, PGC1β is also known to activate mitochondrial biogenesis in cells
250 by activating its target NRF1[42]. Hence, we evaluated PGC1β protein expression in both WT and
251 E50K hRGCs, at different BX795 treatment time points. Interestingly, we observed a significant
252 increase in PGC1β level for WT at 18h while for E50K hRGCs the response was quick, and it
253 remained high during 1h to 18h BX795 treatment and returned back to the basal level at 24h of
254 treatment (**Supplementary Fig. 4 a-c)**. These data suggest pharmacological inhibition of TBK1

255 promotes mitobiogenesis in hRGCs, however, for the glaucomatous E50K mutation such
256 activation could be independent of the AMPKα-PGC1α pathway.

257 **Mitochondrial ultrastructure reveals TBK1 inhibition improves mitochondrial**
258 **coverage and swelling in E50K hRGCs.** Our data showed that E50K hRGCs possess less
259 mitochondrial mass than the WT neurons (**Fig. 4a, b; Supplementary Fig. 3**). However, RGCs
260 are highly metabolically active, so it is possible that in E50K hRGCs each mitochondrion needs
261 to produce more ATP to meet the metabolic need. Studies have shown that a mild increase of the
262 mitochondrial matrix volume (swelling) can help expand the inner mitochondrial membrane (IMM),
263 which in turn stimulates the electron transport chain activity and helps increase production of
264 ATP[43–45]. Such mitochondrial swelling could be physiological and achieved through the prolonged
265 opening of the permeability transition pores (PTP) in the IMM[46]. We asked if such a mechanism
266 is in place for the E50K hRGCs and performed transmission electron microscopy (TEM) to resolve
267 mitochondrial ultrastructure. As a validation to lower mitochondrial mass in E50K hRGCs by
268 immunofluorescence we also observed reduced mitochondrial coverage (mitochondrial section
269 area per unit area of cytoplasm) in glaucomatous E50K hRGCs compared to WT hRGCs (**Fig. 5**
270 **a, b)**. Interestingly, we observed significantly higher perimeter, major and minor axis lengths for
271 the E50K hRGCs in the basal condition (**Fig. 5 c-e**) indicative of swelling which potentially helps
272 mitochondrion to produce more ATP. In support of BX795 mediated activation of mitochondrial
273 biogenesis, TEM analysis further revealed increased mitochondrial coverage in both the WT and
274 E50K hRGCs under BX795 treatment (**Fig. 5 a, b)**. We asked if increased mitochondrial mass by
275 BX795 could reduce ATP production load and hence mitigates swelling in the E50K hRGCs.
276 Indeed, we observed a significant reduction in the mitochondrial perimeter (**Fig. 5c**), major axis
277 length (**Fig. 5d**) and moderate reduction of the minor axis length (**Fig. 5e**) for E50K but not for
278 WT hRGCs in presence of BX795.

279 **TBK1 inhibition restores energy homeostasis and provides neuroprotection for**
280 **E50K hRGCs.** Our data shows that TBK1 inhibition enhances mitochondrial biogenesis and

281 mitigates mitochondria swelling in E50K hRGCs. We asked if these improvements are due to the
282 reduced metabolic burden on mitochondria. To test this, we measured cellular metabolisms
283 corresponding to mitochondrial OXPHOS and glycolysis in both WT and glaucomatous E50K
284 hRGCs using the Seahorse analyzer under control and BX795 treatments. To measure cellular
285 ATP production rate at the basal level, we performed ATP rate assay and surprisingly identified
286 E50K hRGCs both under control (DMSO) and in presence of BX795 showed higher oxygen
287 consumption rate (OCR) than that of WT; however, BX795 treatment itself did not change OCR
288 (**Fig. 6a**). Correspondingly, we observed increased total and mitoATP production rates in E50K
289 hRGCs compared to the WT under control and BX795 treatments (**Fig. 6b**). It has been reported
290 that cellular stress could activate oxidative phosphorylation and increase OCR[47], suggesting
291 increased cellular stress in the glaucomatous E50K hRGCs. Interestingly, we also observed
292 increased glycoATP production rate in the E50K hRGCs compared to WT under BX795 treatment
293 (**Fig. 6b**), presumably due to the high OCR and activation of aerobic glycolysis which is often
294 observed in a variety of cell types[48]. BX795 increased mitochondrial mass in the WT and E50K
295 hRGCs, but it did not alter OCR compared to the DMSO control (**Fig. 6a**). This observation could
296 be supported if the consumed oxygen (OCR) is distributed among an increased number of
297 mitochondria, which will lead to reduced mitoOCR under BX795 treatment to maintain energy
298 homeostasis. To test this, we performed glycolytic rate assay where serial inhibition of
299 mitochondrial activity by rotenone plus antimycin A results in decreased OCR (**Fig. 6c**) and
300 glycolysis inhibition by glucose analogue 2-deoxy-d-glucose (2-DG) results in reduced proton
301 efflux rate (PER) (**Fig. 6d**). These parameters are used to extract mitoOCR and glycoPER for
302 their respective contributions. In support of the higher mitoATP production rate in ATP rate assay
303 (**Fig. 6b**) we also observed increased mitoOCR/glycoPER in the E50K hRGCs compared to the
304 WT cells at the basal level (**Fig. 6e**). Furthermore, we also observed reduced mitoOCR/glycoPER
305 in the E50K hRGCs under BX795 treatment (**Fig. 6e**). This supports the notion that increased
306 mitochondrial mass lowers mitoOCR to maintain energy homeostasis. This data is further

307 supported by the observation that in E50K hRGCs mitochondrial swelling got reduced under
308 BX795 treatment (**Fig. 5c-e**), presumably due to the lower ATP production load per
309 mitochondrion. We next performed a Mito Stress Test to study if increased mitochondrial mass
310 under BX795 treatment helps to combat degenerative conditions as an indication for
311 neuroprotection. In agreement to above results, at the basal level BX795 treatment maintained
312 similar OCR for both the WT (**Fig. 6f**) and E50K hRGCs (**Fig. 6g**). However, under FCCP induced
313 maximum respiration, we observed increased OCR under BX795 treatment for both the WT and
314 E50K hRGCs (**Fig. 6f, g**). This led to an increased spare respiratory capacity (difference between
315 maximal and basal respiration) for both WT and glaucomatous hRGCs when treated with BX795
316 (**Fig. 6h**). An increase in spare respiratory capacity reflects cells' ability to produce additional ATP
317 by OXPHOS to combat degenerative conditions[49]. This suggests TBK1 inhibition mediated
318 activation of mitochondrial biogenesis could confer neuroprotection to the ganglion cells.

319 RGCs are progressively degenerating neurons which exacerbates during aging and under
320 disease conditions[5]. Apoptotic RGC death is the hallmark for glaucoma irrespective of the causal
321 factors[50]. To test if BX795 promotes a pro-survival effect, we measured apoptosis master
322 regulator Caspase-3/7 activity in the WT and E50K hRGCs under basal and CCCP induced
323 damage. Remarkably, we observed 24h of BX795 treatment reduced Caspase activity for the WT
324 and E50K hRGCs both under basal and CCCP damage (**Fig. 6i, k**). We did not observe any
325 increase in Caspase activity for the WT hRGCs even after 48h of CCCP treatment with no
326 additional effect of BX795 (**Fig. 6j**) presumably due to the existence of stringent MQC
327 mechanisms. However, glaucomatous E50K hRGCs showed strong increase in caspase activity
328 post 48h of CCCP treatment which is mitigated by the BX795 treatment (**Fig. 6l**) as evidence for
329 neuroprotection. Furthermore, 48h of BX795 also reduced basal Caspase activity in E50K hRGCs
330 as an indication for sustained neuroprotection under glaucomatous condition.

331 Neurodegenerative diseases are often associated with the protein aggregation[51] and it has been
332 reported that in cultured HEK293 cells $OPTN^{E50K}$ protein forms insoluble aggregates which were

333 dissolved by BX795 drug[52]. Crystal structure analysis revealed the OPTN^{E50K} protein forms tight
334 electrostatic interactions with the E698 residue of TBK1 protein resulting in insoluble
335 aggregates[53,54]. However, the mechanism of BX795 mediated OPTN^{E50K} aggregate dissolution is
336 yet to be discovered. We asked if OPTN^{E50K} forms these insoluble aggregates in hRGCs, and if
337 they could be dissolved by inhibiting TBK1 with BX795. Indeed, by confocal immunofluorescence
338 we observed larger OPTN aggregates in the E50K-hRGCs compared to WT cells, which were
339 then dissolved by TBK1 inhibition using BX795 (**Supplementary Fig. 5a, b)**. Thus, our finding of
340 reduced cellular apoptosis in the E50K hRGCs under BX795 treatment may be a combined effect
341 of restoring energy homeostasis and aggregate dissolution.

342 **Discussion**

343 In this study, we have identified mitochondrial biogenesis as a critical step of MQC which
344 can be activated to promote cell survival for both the WT and glaucomatous E50K RGCs. RGCs
345 are highly sensitive towards mitochondrial damage as they need a steady source of ATP for
346 spontaneous action potential firing[55]. Mitochondrial damage potentially disrupts ATP supply and
347 triggers an energy sensing pathway through AMPK[34]. We have shown here acute damage to
348 mitochondria activates mitochondrial biogenesis in RGCs with robust clearance of damaged
349 mitochondria to maintain mitochondrial homeostasis and energy supply. Activation of this
350 biogenesis occurs through the AMPK-PGC-1α biogenesis axis. Previously, it was reported that
351 the mitochondrial biogenesis activation could be pro-survival as it associates with exercise
352 induced muscle growth[32] and synaptic plasiticity[33]. In support to this notion, we found a robust
353 increase of mitochondrial biogenesis in RGCs with minimal cell death under mitochondrial stress
354 as we previously reported[22].

355 Degradation of damaged mitochondria and biogenesis of healthy organelle are central to
356 the maintenance of energy homeostasis, which is critical for neuronal health. AMPK functions as
357 an energy sensor and responds to energy stress by activating mitochondrial biogenesis[34,56,57]. It
358 has been shown in mice adipose tissue that TBK1 inhibits AMPK activity causing suppression of

359 energy expenditure, obesity, and inflammation[14]. TBK1 is also a key effector for cellular
360 inflammation in response to pro-inflammatory stimuli, and TBK1 inhibition leads to reduced
361 obesity, inflammation, insulin resistance and more energy expenditure in mice in response to a
362 high-fat diet[14]. There are several AMPK activators currently under clinical trials for metabolic
363 diseases[58]. Among them metformin is widely used for type 2 diabetes, however the drug functions
364 through inhibiting mitochondrial complex I which reduces ATP production[58]. Our study provides
365 an indirect activation mechanism of AMPK by targeting TBK1 without compromising mitochondrial
366 function. Thus, TBK1 provides a very interesting target for developing neuroprotection through
367 restoring energy homeostasis which remains unexplored for CNS disorders. We have shown here
368 that TBK1 inhibition by BX795 leads to increased mitochondrial biogenesis in both the WT and
369 glaucomatous (E50K) hRGCs. Interestingly, in WT hRGCs, but not in E50K hRGCs, above
370 treatment activated the AMPKα -PGC1α mito-biogenesis signaling axis. However, PGC1β protein
371 level increased in both the WT and E50K hRGCs under BX795 treatment suggesting existence
372 of PGC1α independent biogenesis activation pathway. It has also been reported that mito-
373 biogenesis could be activated independent of AMPK and PGC1α[59,60], however further studies will
374 be required to delineate the mechanisms of TBK1 inhibition mediated activation of mitochondrial
375 biogenesis in the E50K hRGCs. Increased mitochondrial mass by BX795 restored energy
376 homeostasis, reduced mitochondrial swelling, and enhanced spare respiratory capacity in the
377 E50K hRGCs as an indication for neuroprotection. Remarkably, BX795 treatment not only
378 reduced cellular apoptosis at the basal level but also under CCCP induced apoptosis in the E50K
379 hRGCs, making it a strong candidate for OPTN associated glaucoma neuroprotection therapy. It
380 is intriguing to see that BX795 treatment to the WT hRGCs also increased spare respiratory
381 capacity and reduced cellular apoptosis both under basal and CCCP induced acute mitochondrial
382 damage. Activation of pro-survival pathways under basal conditions in the WT hRGCs in response
383 to TBK1 inhibition suggests these neurons are not in a homeostatic condition. However, it is

384 known RGCs are spontaneously degenerating neurons with reduced mitochondrial function[5,61].
385 Thus, these findings become more important particularly for developing RGC protection for optic
386 neuropathies where no obvious genetic disorders are associated, such as during aging and in
387 high intra-ocular pressure induced glaucoma. Of note, TBK1 copy number increase mutations are
388 found among the normal-tension glaucoma patients[62]. This may lead to reduced mitochondrial
389 biogenesis and disrupted energy homeostasis related RGC death. Our study provides a
390 therapeutic strategy where TBK1 inhibition could promote mitochondrial homeostasis mediated
391 RGC neuroprotection for the above glaucoma conditions.

392 Conflicting evidence suggest TBK1 inhibition could activate[14,63] or inhibit[64] cellular
393 inflammation and activation of inflammation can lead to cell death. As TBK1 inhibition resulted in
394 increased RGC survival, it is unlikely to activate inflammation. TBK1 activity is also critical for
395 activating the mitophagy proteins such as OPTN, NDP52, TAX1BP1 and P62 for successful
396 mitophagy[65] and defects in mitophagy could lead to neurodegeneration[66]. However, it has also
397 been reported that activation of the above mitophagy proteins could occur independent of TBK1,
398 but through ULK1 kinase[67]. Thus, the neuroprotective effect of TBK1 inhibition is unlikely to cause
399 mitophagy defects.

400 Mitochondrial dysfunction is the root cause for optic neuropathies such as LHON, DOA[2]
401 and some cases of glaucoma[9]. Our study provides a neuroprotection strategy for a broad range
402 of optic neuropathies irrespective of the genetic disorders. Severe mitochondrial abnormality has
403 been reported for dopaminergic neurons[3] and motor neurons[4] in PD and ALS respectively. Our
404 study could be applied to test if TBK1 inhibition leads to increased mitochondrial homeostasis and
405 neuroprotection for these CNS disorders.

406

407 **Acknowledgements**

408

409 We thank the Broxmeyer laboratory and the Hypoxia Core Facility of the Indiana University
410 Cooperative Center for Excellence in Hematology (U54 DK106846) for their helpful discussion
411 and assistance in Seahorse experiments; D. Zack for valuable discussions and H7-hESC reporter
412 line; C. Miller from Electron Microscopy Core for sample processing and TEM imaging; and G.
413 Eckert for providing consultations on statistical analysis. This project was funded by grant from
414 the National Institutes of Health, USA (R00EY028223 to A. D and R01033022 to J. M.). This work
415 was supported in part by a Challenge Grant from Research to Prevent Blindness to the
416 Department of Ophthalmology, Indiana University School of Medicine, by the Indiana Clinical and
417 Translational Sciences Institute; by an award from The Glaucoma Foundation (TGF) to A. D., by
418 an award from Ralph W. and Grace M. Showalter Research Trust and the Indiana University
419 School of Medicine to A. D and by BrightFocus foundation (G2020369 to J. M.). The work was
420 funded in part by the Paul and Carole Stark Fellowship and Grants in aid of research from Sigma
421 Xi - The Scientific Research Honor Society, to the graduate student K. A., by the Short-Term
422 Training in Ophthalmology Research for Medical Students funded, in part by T35EY031282 from
423 the National Institutes of Health. The content is solely the responsibility of the authors and does
424 not necessarily represent the official views of the National Institutes of Health.
425

426 **Author contributions**

427 A.D. conceived and supervised the project. A.D., M.S., K.A., S. D., L.J.O. designed and performed
428 experiments and analyzed data. K.C.H., and J.M. developed the E50K reporter lines and
429 contributed to experimental designs. M.S., K.A. and A.D wrote the manuscript.
430

431 **Competing interests**

432 The Authors declare no competing interests.
433

434 **Additional information**

435 **Supplementary information** is available online.

436 **Correspondence and requests for materials** should be directed to Arupratan Das
437 (arupdas@iu.edu)

438 **Methods**

439 **Reagents and resources:** All the reagents including qPCR primers, antibodies and software
440 used are listed in the Supplementary table 1

441

442 **ESC maintenance:**

443 Human embryonic stem cell (H7-hESCs; WiCell, Madison, WI, https://www. wicell.org) reporter
444 line with CRISPR engineered multicistronic BRN3B-P2A-tdTomato-P2A-Thy1.2 construct into the
445 endogenous RGC specific BRN3B locus was used for isogenic control. CRISPR mutated H7-
446 hESC reporter with $OPTN^{E50K\text{-}homozygous}$ mutation (H7-E50K) was done as explained previously[24].
447 Patient derived induced pluripotent stem cells (iPSCs) with E50K mutation[23] (iPSC-E50K), E50K
448 mutation corrected to WT by CRISPR in the patient derived iPSC (iPSC-E50Kcorr)[24] with
449 BRN3B::tdTomato reporter were obtained from the Jason Meyer lab. All the above cell lines were
450 grown in mTeSR1 media (mT) at 37°C in 5% CO_2 incubator on matrigel (MG) coated plates. These
451 cells were maintained by clump passaging using Gentle Cell Dissociation Reagent (GD) after 70-
452 80% confluency. Media was aspirated and GD was added to cells followed by incubation at 37°C
453 in 5% CO_2 incubator for 5 minutes. Next, mT was used to break up the colonies into small clumps
454 by repeated pipetting and then seeded onto new MG plates.

455

456 **hRGC differentiation and immunopurification:**

457 For differentiation, stem cells were dissociated to single cells using accutase for 10 min and then
458 quenched with twice the volume of mT with 5 μM blebbistatin (blebb). The cells were centrifuged
459 at 150 G for 6 minutes and resuspended in mT with 5 μM blebb. 100,000 cells were seeded per

460 well of a 24-well MG coated plate. The next day, media was replaced with mT without blebb. After
461 24 hours, media was replaced with differentiation media (iNS) and further small molecule-based
462 differentiation was carried out with iNS media as elucidated previously[22]. hRGC differentiation
463 was monitored by tdTomato expression and cells were purified during days 45-55 using THY1.2
464 microbeads and magnetic activated cell sorting system (MACS, Miltenyi Biotec) as explained
465 before[19,22]. hRGCs were resuspended in iNS media, counted using a hemocytometer and seeded
466 on MG coated plates, coverslips, or MatTek dishes for experiments.
467
468 **Flow Cytometry**
469 Purified hRGCs were seeded at 30,000 cells per well of a 96-well MG coated plate and maintained
470 for 3 days. For measuring mitochondrial mass, hRGCs were labeled with mitochondria specific
471 MTDR dye. To measure mitochondrial degradation, hRGCs were labeled with 10 nM MTDR dye
472 for 1 hour, washed, and then treated with 10 μM CCCP for a time course. To measure
473 mitochondrial biogenesis, hRGCs were labeled with MTDR first, then treated with 10 μM CCCP
474 or equal amount of DMSO for 3 hours, then washed and incubated with fresh media with MTDR
475 for the time course. After treatments, hRGCs were dissociated to single cell suspension using
476 accutase and analyzed using Attune NxT flow cytometer (Thermo Fisher).
477
478 **Western Blot:**
479 Purified hRGCs were seeded at 500,000 cells per well of 24-well MG coated plates and
480 maintained for 3 days. The cells were then treated (10 μM CCCP, 1 μg/ml BX795 or equivalent
481 volume of DMSO) for the designated durations. DMSO was used as the control as the small
482 molecules were dissolved in DMSO. The cells were lysed and collected in 100 μl of M-PER
483 extraction buffer with 5 mM EDTA and protease inhibitors. Protein quantification was done using
484 a BSA standard following the DC Protein Assay Kit II (Bio-Rad) and read on microplate reader.
485 Loading samples were prepared with heat denaturation at 95°C for 5 minutes with laemmli sample

486 buffer (1X). 10-20 µg protein per sample were run on Bio-Rad Mini-PROTEAN TGX precast gels,
487 in running buffer (Tris-Glycine-SDS buffer; Bio-Rad) at 100V until the dye front reached to the
488 bottom. The transfer sandwich was made using PVDF membrane (activated in methanol) in Tris-
489 Glycine transfer buffer (Bio-Rad) with 20% methanol and transferred for 2 hours at 30V, 4ºC. For
490 the visualization of proteins, the membranes were blocked in 5% skim milk in TBST (TBS buffer
491 with 20% Tween20) for 2 hours at room temperature and incubated overnight at 4°C in 1:1000
492 dilution of primary antibodies for PGC1α (Abcam), Phospho-PGC1α^{Ser571} (R&D Systems), PGC1β
493 (Abcam), AMPKα (Cell Signaling Technologies, CST), Phospho-AMPKα^{Thr172} (CST), LC3B
494 (Sigma), GAPDH (CST), or ACTIN (CST). Membranes were then washed 3 times for 5 minutes
495 each in TBST, followed by 2 hours of incubation in 5% milk in TBST containing anti-rabbit HRP
496 linked secondary antibody (CST) at 1:10,000 dilution. The membrane was again washed 3 times
497 with TBST and then placed in Clarity Max Western ECL (Bio-Rad) substrate for 5 minutes. The
498 membranes were imaged in a Bio-Rad ChemiDoc Gel Imager, and the raw integrated density for
499 each band was measured and normalized with respect to the corresponding GAPDH or actin
500 loading control using image J. Treatment conditions were further normalized to the corresponding
501 DMSO control for each experiment. Complete blots of the representative western blot images,
502 with protein molecular weight marker (Thermo Scientific), are provided in **Supplementary fig. 6.**
503 Protein bands corresponding to the appropriate size were quantified following product datasheets
504 and published literature.
505
506 **Immunofluorescence and Confocal imaging:**
507 Purified hRGCs were seeded on MG coated coverslips (1.5 thickness) at a density of 30,000 -
508 40,000 cells per coverslip and grown for 3 days. hRGCs were then treated (10 μM CCCP, 1 μg/ml
509 BX795 or equivalent volume of vehicle control DMSO), for the indicated time points. After
510 treatment the media was aspirated, the cells were washed with 1X PBS, and then fixed with 4%
511 Paraformaldehyde for 15 min at 37ºC. Fixed cells were permeabilized with 0.5% Triton-X100 in

512 PBS for 5 min and then washed with washing buffer (1% donkey serum, 0.05% Triton-X100 in
513 PBS) 3 times for 5 minutes each. Cells were blocked with blocking buffer (5% donkey serum,
514 0.2% Triton-X100 in PBS) for 1 hour. After blocking, antibodies against Tom20 (Mouse, Santa
515 Cruz) and Optineurin (Rabbit, Cayman Chemicals) were added (1:200 in blocking buffer) and the
516 coverslips were incubated overnight at 4°C. Next, coverslips were washed with washing buffer 3
517 times for 5 minutes each and incubated for 2 hours at room temperature in the dark with
518 secondary antibodies, donkey anti-mouse Alexa-488 (Invitrogen) and anti-rabbit Alexa-647
519 (Invitrogen) (1:500). The coverslips were washed with washing buffer 3 times for 5 minutes each,
520 with 1.43 μM DAPI added to the second wash. The coverslips were then mounted onto slides with
521 DAKO. Visualization of mitochondria and optineurin (OPTN) aggregates was done by confocal
522 immunofluorescence. Z-stacks of cells were taken using Zeiss LSM700 with 63x/1.4 oil objective.
523 Analysis was carried out using ImageJ with maximum projections of DAPI channel (number of
524 nuclei) and sum projections of TOM20 and OPTN channels. For OPTN aggregate size, we
525 analyzed particles from 0.02 a.u. to infinity to account for the small and big aggregates.
526
527 **qPCR:**
528 Purified hRGCs were seeded at 300,000 cells per well of 24-well MG coated plates and
529 maintained for 3 days. Cells were then treated (10 μM CCCP, 1 μg/ml BX795 or equivalent volume
530 of DMSO) for the designated durations. Media was aspirated and cells were incubated in 200 μl
531 accutase for 10 min and then quenched with 400 μl iNS media. Cells were centrifuged at 150 G
532 for 6 min, media aspirated, and the cell pellets were stored at -20°C. RNA was extracted from cell
533 pellets following the kit protocol (Qiagen 74104). The RNA concentration was measured using
534 Nanodrop 2000c (Thermo) and 6 μl of RNA was used to prepare cDNA following the kit protocol
535 (Abm #G492). qPCR primers were designed as detailed in Table S1. qPCR was performed using
536 BlasTaq qPCR MasterMix with 100 ng total cDNA in a 20 μl reaction mixture using QuantStudio6
537 Flex RT PCR system (Applied Biosystems). GAPDH or actin was used as a housekeeping gene

538 in every plate to calculate the ΔCt values. The ΔΔCt was calculated with respect to (w.r.t) the
539 average ΔCt of the control sample. All conditions were measured by averaging 3 technical repeats
540 for each biological repeat with total 3 biological replicates.

541 **Mitochondrial DNA measurements by qPCR**

542 Purified hRGCs were seeded at 50,000-75,000 cells per well of 96-well MG coated plates and
543 maintained for 3 days. Cells were then treated (10 μM CCCP, 1 μg/ml BX795 or equivalent volume
544 of DMSO) for the designated durations. Media was aspirated and cells were incubated in 30 µl
545 accutase for 10 min and then quenched with 100 µl iNS media. Cells were centrifuged at 150 G
546 for 6 min, media aspirated, and the cell pellets were stored at -20°C. DNA was extracted using
547 DNeasy Blood & Tissue Kit (Qiagen) and eluted with 30 µl elution buffer. DNA concentration was
548 measured using Nanodrop 2000c (Thermo). 10 ng of DNA was used to measure both
549 mitochondrial ND1 gene and internal control, human nuclear RNase P gene copy numbers, as
550 done previously[22].
551

552 **JC1 imaging:**

553 hRGCs were seeded in MG coated MatTek dishes at 40,000 cells per dish and maintained for 3
554 days. For the first experiment (Fig. 2 a-c), cells were incubated with 250 μl of JC1 media (1:100
555 in iNS) for 30 min in the incubator, then an additional 1.75 ml of dilute JC1 (1:1000 in iNS) was
556 added to the dish. The dish was then transferred to the live cell chamber (5% CO^2, 37°C, Tokai
557 Hit) and confocal images were acquired prior to (before) and 10 minutes after CCCP (10 μM)
558 treatment using Zeiss LSM700 with 63x/1.4 oil objective. The second experiment (Fig 2 d-f) cells
559 were treated with 10 μM CCCP or equivalent DMSO for 30 minutes. Media with treatment was
560 removed, cells were washed, and then incubated with 250 ul of JC1 media (1:100 in iNS) for 30
561 min in the incubator. The JC1 media was then removed, cells were washed again, and 2 ml of

562 new iNS was added to the dish. The dish was then transferred to the live cell chamber and
563 imaged. Analysis was carried out using ImageJ with sum projections of red and green channels.
564 The red fluorescence from the tdTomato expressed by the hRGCs was much less intense than
565 the JC1 red staining of mitochondria, thus the red fluorescence measured from the cytoplasm
566 was considered background and subtracted out of the measurements. For the green
567 fluorescence, background was measured from outside the cell. Red:Green ratio was calculated
568 by dividing the red intensity by green intensity; these values were then normalized to the control,
569 H7WT-before (Fig 2 a-c) or average DMSO ratio at that timepoint for each cell line (Fig 2 d-f).
570
571 **Seahorse analysis:**
572 The 96-well seahorse plate was coated with MG and hRGCs were seeded at 250,000 cells per
573 well and maintained for 2 days. 24 hours before measurements, media was exchanged with 100
574 µl iNS with 1 µg/ml BX795 or equivalent vehicle control DMSO. A day prior to the assay, the
575 sensor cartridge was fully submerged with 200 µl of sterile water to hydrate it overnight in a non-
576 CO_2, 37°C incubator. The next day, sterile water was replaced with pre-warmed XF calibrant
577 buffer and the sensors were again submerged and incubated in the non-CO_2, 37°C incubator for
578 45-60 minutes. Seahorse media was made by adding stock solutions to seahorse media (XF
579 DMEM) to have final concentrations of 21.25 mM glucose, 0.36 mM sodium pyruvate, and 1.25
580 mM L-glutamine (Agilent), with pH adjusted to 7.38-7.42. Depending upon the assay, 20 µM
581 Oligomycin (Oligo), 20 µM FCCP, 2.5 µg/ml Rotenone plus 5 µM Antimycin A (Rot/AA), and/or
582 175 mM 2-Deoxy-D-glucose (2-DG) solutions were then prepared in Seahorse media. In the
583 hRGC seahorse plate, iNS media was carefully exchanged to seahorse media by removing, 60
584 µl iNS from all wells and adding 140 µl of Seahorse media. Next, 140 µl of the mixed media was
585 removed by pipette and then an additional 140 µl seahorse media was added to each well to have
586 a final volume of 180 µl. 180 µl of Seahorse media was then added to any empty wells. The plate
587 was placed in Incucyte S3 (Sartorius) and one image of each well was taken for cell area

588 normalization using brightfield and red fluorescence (tdTomato) channels. The hRGC seahorse
589 plate was then placed into a non-CO_2, 37°C incubator for at least 45 min. The reagents were
590 added into their respective ports in the cartridge with the final concentrations in the wells; for ATP
591 rate assay of 2.0 μM Oligo and 0.25 μg/ml Rotenone plus 0.5 μM Antimycin A; for the glycolytic
592 rate assay of 0.25 μg/ml Rotenone plus 0.5 μM Antimycin A and 17.5 mM 2-DG; and for the Mito
593 stress test of 2.0 μM Oligo, 2.0 μM FCCP (optimal concentration from FCCP titration), and 0.25
594 μg/ml Rotenone plus 0.5 μM Antimycin A. After loading all ports, the cartridge was placed into a
595 non-CO_2, 37°C incubator while the experiment was setup in WAVE software (Agilent). The
596 cartridge was then placed into the XFe96 analyzer (Agilent) and run for calibration. After the
597 machine calibrations were successful, the hRGC seahorse plate was placed into the machine and
598 the assay was run (ATP rate assay, glycolytic rate assay, or Mito stress test). Cell area from
599 incucyte images were measured using image J and extrapolated for the total cell area in each
600 well for normalization. The assay results were then exported into the appropriate excel macro
601 using Seahorse Wave Desktop software (Agilent) for analysis.
602
603 **Caspase activity:**
604 hRGCs were seeded at 25,000 cells per well of a 96-well clear bottom black walled plate and
605 maintained for 3 days. The cells were then treated with 1 μg/ml BX795 or equivalent volume of
606 DMSO vehicle control for 24 hours. The caspase activity was measured using the ApoTox-Glo
607 Triplex assay kit (Promega). Assay buffer, GF-AFC substrate and bis-AAF-R110 substrate were
608 thawed at 37°C and 10μl of GF-AFC substrate and bis-AAF-R110 substrate were added into 2.0
609 ml of assay buffer and vortexed until dissolved to make the viability-cytotoxicity reagent. 20μl of
610 viability-cytotoxicity reagent was added to all wells, and briefly mixed. The plate was incubated at
611 37°C for 30 minutes before measuring the fluorescence at 400nm/505nm (Ex/Em) for viability.
612 Next, 100 μl of Caspase-Glo® 3/7 reagent was added to all wells and incubated for 30 minutes

613 at room temperature before measuring luminescence (Caspase). Measurements were
614 normalized to DMSO control.
615
616 **Electron Microscopy:**
617 hRGCs were seeded at 250,000 cells per well on MG coated 6-well plates and maintained for 3
618 days. The cells were then treated with 1 μg/ml BX795 or equivalent DMSO for 24 hours. Media
619 was aspirated, 500 μl of fixative solution (3% Glutaraldehyde, 0.1 M Cacodylate) was added, and
620 the cells were incubated for 15 minutes. hRGCs were then scraped and pelleted by centrifugation
621 at 10,000 G for 20 minutes. The pellets were fixed overnight at 4°C, then rinsed the next day in
622 0.1 M cacodylate buffer, followed by post fixation with 1% osmium tetroxide, 0.1 M cacodylate
623 buffer for 1 hour. After rinsing again with 0.1 M cacodylate buffer, the cell pellets were dehydrated
624 through a series of graded ethyl alcohols from 70 to 100%, and 2 changes of 100% acetone. The
625 cell pellets were then infiltrated with a 50:50 mixture of acetone and embedding resin (Embed
626 812, Electron Microscopy Sciences, Hatfield, PA) for 72 hours. Specimen vial lids were then
627 removed, and acetone allowed to evaporate off for 3 hours. Then the pellets were embedded in
628 a fresh change of 100% embedding resin. Following polymerization overnight at 60°C the blocks
629 were then ready for sectioning. All procedures were done in centrifuge tubes including the final
630 embedding. Sections with cut at 85nm, placed on copper grids, stained with saturated uranyl
631 acetate, viewed, and imaged on a Tecnai Spirit (ThermoFisher, Hillsboro, OR) equipped with an
632 AMT CCD camera (Advanced Microscopy Techniques, Danvers, MA). 49000X images were
633 analyzed using Image J to measure mitochondrial characteristics and then normalized to
634 cytoplasmic area (mitochondrial number and area) or ratio of major to minor axis for aspect ratio.
635
636 **Quantification and Statistical analysis:**

Samples were treated with CCCP or BX795 at different time points as independent biological samples. Statistical tests between two independent datasets were done by Student's *t-test*, each data point within a dataset is from an independent culture well (Fig.1c-f, 1h, 1m; 1j, 1l, 2c, 2f, 3a-d, 3f-i, 4b-d, 4f-i, 5b, 6b, 6e, 6h-l, Supp Fig. 3b, 4b-c). We used *t-test* rather than ANOVA because we did not want to assume that each group has the same variance. For non-normal data distribution, we performed Mann Whitney U test to compare between two independent data sets (Fig. 5c-e, Supp Fig. 5b). Graphs were made using GraphPad Prism 9.0 software.

Data availability

All cell lines and data used during the current study are available from the corresponding author upon reasonable request.

Code availability

Data analyzed using commercially available software, no code has been developed for the current study.

References:

1. Kann, O. & Kovács, R. Mitochondria and neuronal activity. *American Journal of Physiology - Cell Physiology* vol. 292 Preprint at https://doi.org/10.1152/ajpcell.00222.2006 (2007).
2. Yu-Wai-Man, P., Griffiths, P. G. & Chinnery, P. F. Mitochondrial optic neuropathies - Disease mechanisms and therapeutic strategies. *Progress in Retinal and Eye Research* vol. 30 81–114 Preprint at https://doi.org/10.1016/j.preteyeres.2010.11.002 (2011).
3. Reeve, A. K. *et al.* Mitochondrial dysfunction within the synapses of substantia nigra neurons in Parkinson's disease. *NPJ Parkinsons Dis* **4**, (2018).
4. Kong, J. & Xu, Z. Massive mitochondrial degeneration in motor neurons triggers the onset of amyotrophic lateral sclerosis in mice expressing a mutant SOD1. *Journal of Neuroscience* **18**, (1998).
5. Quigley, H. A. Understanding Glaucomatous Optic Neuropathy: The Synergy Between Clinical Observation and Investigation. *Annual review of vision science* vol. 2 235–254 Preprint at https://doi.org/10.1146/annurev-vision-111815-114417 (2016).

669 6. Neishabouri, A. & Faisal, A. A. Saltatory conduction in unmyelinated axons: Clustering of
670 Na+ channels on lipid rafts enables micro-saltatory conduction in C-fibers. *Front*
671 *Neuroanat* **8**, (2014).
672 7. Man, P. Y. W., Turnbull, D. M. & Chinnery, P. F. Leber hereditary optic neuropathy.
673 *Journal of Medical Genetics* vol. 39 Preprint at https://doi.org/10.1136/jmg.39.3.162
674 (2002).
675 8. Zanna, C. *et al.* OPA1 mutations associated with dominant optic atrophy impair oxidative
676 phosphorylation and mitochondrial fusion. *Brain* **131**, (2008).
677 9. Wolf, C. *et al.* Evaluation of nine candidate genes in patients with normal tension
678 glaucoma: A case control study. *BMC Med Genet* **10**, 91 (2009).
679 10. Rezaie, T. *et al.* Adult-onset primary open-angle glaucoma caused by mutations in
680 optineurin. *Science (1979)* **295**, 1077–1079 (2002).
681 11. Ayala-Lugo, R. M. *et al.* Variation in optineurin (OPTN) allele frequencies between and
682 within populations. *Mol Vis* **13**, 151–63 (2007).
683 12. Garcia, D. & Shaw, R. J. AMPK: Mechanisms of Cellular Energy Sensing and Restoration
684 of Metabolic Balance. *Molecular Cell* vol. 66 Preprint at
685 https://doi.org/10.1016/j.molcel.2017.05.032 (2017).
686 13. Salminen, A. & Kaarniranta, K. AMP-activated protein kinase (AMPK) controls the aging
687 process via an integrated signaling network. *Ageing Research Reviews* vol. 11 Preprint at
688 https://doi.org/10.1016/j.arr.2011.12.005 (2012).
689 14. Zhao, P. *et al.* TBK1 at the Crossroads of Inflammation and Energy Homeostasis in
690 Adipose Tissue. *Cell* **172**, 731-743.e12 (2018).
691 15. Mattson, M. P. & Arumugam, T. v. Hallmarks of Brain Aging: Adaptive and Pathological
692 Modification by Metabolic States. *Cell Metabolism* vol. 27 Preprint at
693 https://doi.org/10.1016/j.cmet.2018.05.011 (2018).
694 16. Jäer, S., Handschin, C., St-Pierre, J. & Spiegelman, B. M. AMP-activated protein kinase
695 (AMPK) action in skeletal muscle via direct phosphorylation of PGC-1α. *Proc Natl Acad*
696 *Sci U S A* **104**, (2007).
697 17. Zhao, P. & Saltiel, A. R. Interaction of Adipocyte Metabolic and Immune Functions
698 Through TBK1. *Frontiers in Immunology* vol. 11 Preprint at
699 https://doi.org/10.3389/fimmu.2020.592949 (2020).
700 18. Peng, Y. R. *et al.* Molecular Classification and Comparative Taxonomics of Foveal and
701 Peripheral Cells in Primate Retina. *Cell* **176**, 1222-1237.e22 (2019).
702 19. Sluch, V. M. *et al.* Enhanced Stem Cell Differentiation and Immunopurification of Genome
703 Engineered Human Retinal Ganglion Cells. *Stem Cells Transl Med* **6**, 1972–1986 (2017).
704 20. Sluch, V. M. *et al.* Differentiation of human ESCs to retinal ganglion cells using a CRISPR
705 engineered reporter cell line. *Sci Rep* **5**, (2015).
706 21. Zhang, K. Y. *et al.* Role of the Internal Limiting Membrane in Structural Engraftment and
707 Topographic Spacing of Transplanted Human Stem Cell-Derived Retinal Ganglion Cells.
708 *Stem Cell Reports* **16**, 149–167 (2021).
709 22. Das, A., Bell, C. M., Berlinicke, C. A., Marsh-Armstrong, N. & Zack, D. J. Programmed
710 switch in the mitochondrial degradation pathways during human retinal ganglion cell
711 differentiation from stem cells is critical for RGC survival. *Redox Biol* (2020)
712 doi:10.1016/j.redox.2020.101465.
713 23. Ohlemacher, S. K. *et al.* Stepwise Differentiation of Retinal Ganglion Cells from Human
714 Pluripotent Stem Cells Enables Analysis of Glaucomatous Neurodegeneration. *Stem*
715 *Cells* **34**, 1553–1562 (2016).
716 24. VanderWall, K. B. *et al.* Retinal Ganglion Cells With a Glaucoma OPTN(E50K) Mutation
717 Exhibit Neurodegenerative Phenotypes when Derived from Three-Dimensional Retinal
718 Organoids. *Stem Cell Reports* **15**, 52–66 (2020).

719 25. Padman, B. S., Bach, M., Lucarelli, G., Prescott, M. & Ramm, G. The protonophore
720 CCCP interferes with lysosomal degradation of autophagic cargo in yeast and
721 mammalian cells. *Autophagy* **9**, (2013).
722 26. Miyazono, Y. *et al.* Uncoupled mitochondria quickly shorten along their long axis to form
723 indented spheroids, instead of rings, in a fission-independent manner. *Sci Rep* **8**, (2018).
724 27. Xiao, B., Deng, X., Zhou, W. & Tan, E. K. Flow cytometry-based assessment of
725 mitophagy using mitotracker. *Frontiers in Cellular Neuroscience* vol. 10 Preprint at
726 https://doi.org/10.3389/fncel.2016.00076 (2016).
727 28. Villa, E., Marchetti, S. & Ricci, J. E. No Parkin Zone: Mitophagy without Parkin. *Trends in*
728 *Cell Biology* vol. 28 882–895 Preprint at https://doi.org/10.1016/j.tcb.2018.07.004 (2018).
729 29. Fujita, N. *et al.* An Atg4B mutant hampers the lipidation of LC3 paralogues and causes
730 defects in autophagosome closure. *Mol Biol Cell* **19**, 4651–4659 (2008).
731 30. Sivandzade, F., Bhalerao, A. & Cucullo, L. Analysis of the Mitochondrial Membrane
732 Potential Using the Cationic JC-1 Dye as a Sensitive Fluorescent Probe. *Bio Protoc* **9**,
733 (2019).
734 31. Buckman, J. F. & Reynolds, I. J. Spontaneous changes in mitochondrial membrane
735 potential in cultured neurons. *Journal of Neuroscience* **21**, (2001).
736 32. Holloszy, J. O. Regulation of mitochondrial biogenesis and GLUT4 expression by
737 exercise. *Comprehensive Physiology* vol. 1 921–940 Preprint at
738 https://doi.org/10.1002/cphy.c100052 (2011).
739 33. Mattson, M. P., Moehl, K., Ghena, N., Schmaedick, M. & Cheng, A. Intermittent metabolic
740 switching, neuroplasticity and brain health. *Nature Reviews Neuroscience* vol. 19 81–94
741 Preprint at https://doi.org/10.1038/nrn.2017.156 (2018).
742 34. Hardie, D. G. AMP-activated protein kinase-an energy sensor that regulates all aspects of
743 cell function. *Genes and Development* vol. 25 1895–1908 Preprint at
744 https://doi.org/10.1101/gad.17420111 (2011).
745 35. Shaw, R. J. *et al.* The tumor suppressor LKB1 kinase directly activates AMP-activated
746 kinase and regulates apoptosis in response to energy stress. *Proc Natl Acad Sci U S A*
747 **101**, 3329–3335 (2004).
748 36. Wu, Z. *et al.* Mechanisms controlling mitochondrial biogenesis and respiration through the
749 thermogenic coactivator PGC-1. *Cell* **98**, 115–124 (1999).
750 37. Gureev, A. P., Shaforostova, E. A. & Popov, V. N. Regulation of mitochondrial biogenesis
751 as a way for active longevity: Interaction between the Nrf2 and PGC-1α signaling
752 pathways. *Frontiers in Genetics* vol. 10 Preprint at
753 https://doi.org/10.3389/fgene.2019.00435 (2019).
754 38. Scarpulla, R. C., Vega, R. B. & Kelly, D. P. Transcriptional integration of mitochondrial
755 biogenesis. *Trends in Endocrinology and Metabolism* vol. 23 459–466 Preprint at
756 https://doi.org/10.1016/j.tem.2012.06.006 (2012).
757 39. Clark, K., Plater, L., Peggie, M. & Cohen, P. Use of the pharmacological inhibitor BX795
758 to study the regulation and physiological roles of TBK1 and IκB Kinase ∈:A distinct
759 upstream kinase mediates ser-172 phosphorylation and activation. *Journal of Biological*
760 *Chemistry* **284**, (2009).
761 40. Minegishi, Y., Nakayama, M., Iejima, D., Kawase, K. & Iwata, T. Significance of optineurin
762 mutations in glaucoma and other diseases. *Progress in Retinal and Eye Research* vol. 55
763 149–181 Preprint at https://doi.org/10.1016/j.preteyeres.2016.08.002 (2016).
764 41. Ma, L. *et al.* Mitochondrial morphology and function impaired by dimethyl sulfoxide and
765 dimethyl Formamide. *J Bioenerg Biomembr* **50**, 297–305 (2018).
766 42. Shao, D. *et al.* PGC-1β-Regulated mitochondrial biogenesis and function in myotubes is
767 mediated by NRF-1 and ERRα. *Mitochondrion* **10**, 516–527 (2010).

43. Halestrap, A. P. The regulation of the matrix volume of mammalian mitochondria in vivo and in vitro and its role in the control of mitochondrial metabolism. *Biochimica et Biophysica Acta (BBA) - Bioenergetics* **973**, 355–382 (1989).
44. Armston, A. E., Halestrap, A. P. & Scott, R. D. The nature of the changes in liver mitochondrial function induced by glucagon treatment of rats. The effects of intramitochondrial volume, aging and benzyl alcohol. *Biochimica et Biophysica Acta (BBA) - Bioenergetics* **681**, 429–439 (1982).
45. Okayasu, T., Curtis, M. T. & Farber, J. L. Structural alterations of the inner mitochondrial membrane in ischemic liver cell injury. *Arch Biochem Biophys* **236**, 638–645 (1985).
46. Javadov, S., Chapa-Dubocq, X. & Makarov, V. Different approaches to modeling analysis of mitochondrial swelling. *Mitochondrion* vol. 38 Preprint at https://doi.org/10.1016/j.mito.2017.08.004 (2018).
47. Hong, X. *et al.* Mitochondrial dynamics maintain muscle stem cell regenerative competence throughout adult life by regulating metabolism and mitophagy. *Cell Stem Cell* **29**, 1298-1314.e10 (2022).
48. Jones, W. & Bianchi, K. Aerobic glycolysis: Beyond proliferation. *Frontiers in Immunology* vol. 6 Preprint at https://doi.org/10.3389/fimmu.2015.00227 (2015).
49. Desler, C. *et al.* Is there a link between mitochondrial reserve respiratory capacity and aging? *Journal of Aging Research* vol. 2012 Preprint at https://doi.org/10.1155/2012/192503 (2012).
50. Qu, J., Wang, D. & Grosskreutz, C. L. Mechanisms of retinal ganglion cell injury and defense in glaucoma. *Exp Eye Res* **91**, (2010).
51. Ross, C. A. & Poirier, M. A. Protein aggregation and neurodegenerative disease. *Nat Med* **10**, S10 (2004).
52. Minegishi, Y. *et al.* Enhancedoptineurin E50k-TBK1 interaction evokes protein insolubility and initiates familial primary open-angle glaucoma. *Hum Mol Genet* **22**, 3559–3567 (2013).
53. Li, F. *et al.* Structural insights into the interaction and disease mechanism of neurodegenerative disease-associated optineurin and TBK1 proteins. *Nat Commun* **7**, (2016).
54. Minegishi, Y. *et al.* Enhancedoptineurin E50k-TBK1 interaction evokes protein insolubility and initiates familial primary open-angle glaucoma. *Hum Mol Genet* **22**, 3559–3567 (2013).
55. Yu, D. Y. *et al.* Retinal ganglion cells: Energetics, compartmentation, axonal transport, cytoskeletons and vulnerability. *Progress in Retinal and Eye Research* vol. 36 Preprint at https://doi.org/10.1016/j.preteyeres.2013.07.001 (2013).
56. Hardie, D. G., Ross, F. A. & Hawley, S. A. AMPK: A nutrient and energy sensor that maintains energy homeostasis. *Nature Reviews Molecular Cell Biology* vol. 13 Preprint at https://doi.org/10.1038/nrm3311 (2012).
57. Daval, M., Foufelle, F. & Ferré, P. Functions of AMP-activated protein kinase in adipose tissue. *Journal of Physiology* vol. 574 Preprint at https://doi.org/10.1113/jphysiol.2006.111484 (2006).
58. Steinberg, G. R. & Carling, D. AMP-activated protein kinase: the current landscape for drug development. *Nature Reviews Drug Discovery* vol. 18 Preprint at https://doi.org/10.1038/s41573-019-0019-2 (2019).
59. Marcinko, K. & Steinberg, G. R. The role of AMPK in controlling metabolism and mitochondrial biogenesis during exercise. *Exp Physiol* **99**, (2014).
60. Xiao, L. *et al.* AMPK-dependent and -independent coordination of mitochondrial function and muscle fiber type by FNIP1. *PLoS Genet* **17**, (2021).
61. Eells, J. T. Mitochondrial dysfunction in the aging retina. *Biology* vol. 8 Preprint at https://doi.org/10.3390/biology8020031 (2019).

819 62. Ritch, R. *et al.* TBK1 gene duplication and normal-tension glaucoma. *JAMA Ophthalmol*
820 **132**, 544–548 (2014).
821 63. Taft, J. *et al.* Human TBK1 deficiency leads to autoinflammation driven by TNF-induced
822 cell death. *Cell* **184**, (2021).
823 64. Reilly, S. M. *et al.* An inhibitor of the protein kinases TBK1 and IKK-ε improves obesity-
824 related metabolic dysfunctions in mice. *Nat Med* **19**, (2013).
825 65. Richter, B. *et al.* Phosphorylation of OPTN by TBK1 enhances its binding to Ub chains
826 and promotes selective autophagy of damaged mitochondria. *Proc Natl Acad Sci U S A*
827 **113**, 4039–4044 (2016).
828 66. Cai, Q. & Jeong, Y. Y. Mitophagy in Alzheimer's Disease and Other Age-Related
829 Neurodegenerative Diseases. *Cells* **9**, 150 (2020).
830 67. Harding, O. *et al.* ALS- And FTD-associated missense mutations in TBK1 differentially
831 disrupt mitophagy. *Proc Natl Acad Sci U S A* **118**, (2021).
832

833

Figure 1

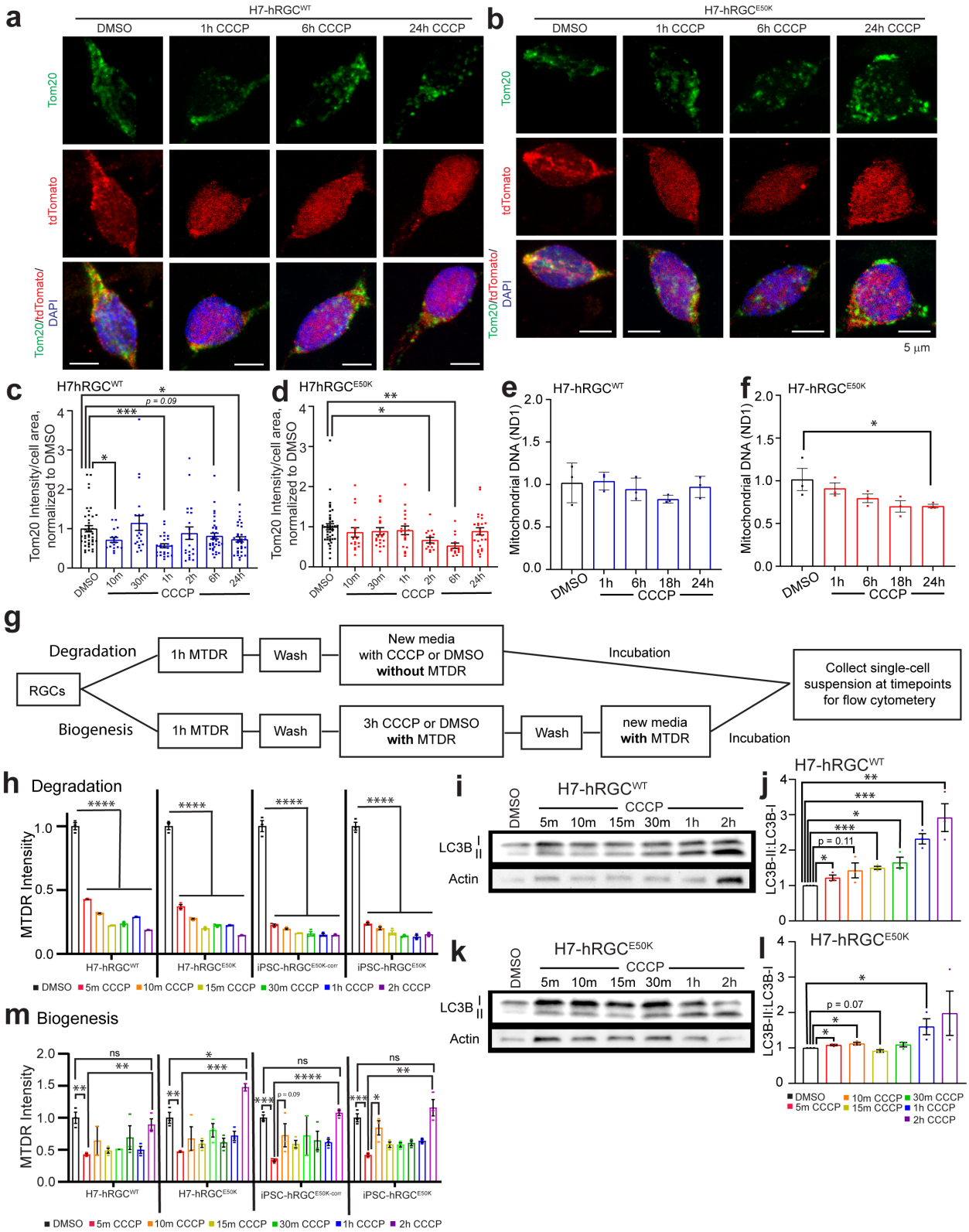
a
H7-hRGC^WT
DMSO
1h CCCP
6h CCCP
24h CCCP
Tom20
tdTomato
Tom20/tdTomato/DAPI
b
H7-hRGC^E50K
5 µm
c
H7hRGC^WT
Tom20 Intensity/cell area, normalized to DMSO
p = 0.09
CCCP
d
H7hRGC^E50K
e
H7-hRGC^WT
Mitochondrial DNA (ND1)
f
H7-hRGC^E50K
g
Degradation
RGCs
1h MTDR
Wash
New media with CCCP or DMSO without MTDR
Incubation
Collect single-cell suspension at timepoints for flow cytometery
Biogenesis
3h CCCP or DMSO with MTDR
new media with MTDR
h Degradation
MTDR Intensity
H7-hRGC^WT
H7-hRGC^E50K
iPSC-hRGC^E50K-corr
iPSC-hRGC^E50K
DMSO 5m CCCP 10m CCCP 15m CCCP 30m CCCP 1h CCCP 2h CCCP
i
LC3B I II
Actin
j
LC3B-II:LC3B-I
p = 0.11
k
l
p = 0.07
m Biogenesis
ns

Figure 1. hRGCs maintain mitochondrial mass by simultaneous degradation and biogenesis of mitochondria under damage. (a, b) Representative confocal immunofluorescence images of H7-hRGCs against mitochondrial Tom20, tdTomato, and DAPI after indicated 10 μM CCCP treatment timepoints. Scale bars are 5 μm. **(c, d)** Quantification of Tom20 intensity per cell area from sum projections of confocal z-stacks, normalized to corresponding DMSO. n=14-42 cells per condition. **(e, f)** Mitochondrial DNA copy number analyzed by qPCR for mitochondrial ND1 gene relative to nuclear RNase P. Results shown as ΔΔCt fold changes relative to DMSO control for different times points of 10 μM CCCP treatment. n=3, 3 technical repeats averaged for each biological repeat. **(g)** Schematic of MTDR flow experiments for tracking degrading versus newly synthesized mitochondria. **(h, m), (h)** Mitochondrial mass in single cells at different CCCP treatment time points for degradation or **(m)** different timepoints post CCCP wash for biogenesis were measured by flow cytometer, and the average fluorescent intensity normalized to DMSO was plotted. n=3. **(i, k)** Representative western blot images of LC3B and actin from **(i)** $hRGC^{WT}$ and **(k)** $hRGC^{E50K}$ treated with CCCP for the indicated timepoints. **(j, l)** Quantification of the ratio of LC3B-II to corresponding LC3B-I for each condition. n = 3. ∗ p-value < 0.05, ∗∗ p-value < 0.01, ∗∗∗ p-value < 0.001, ∗∗∗∗ p-value < 0.0001. Unpaired student's *t-test* between independent datasets. Error bars are SEM.

Figure 2

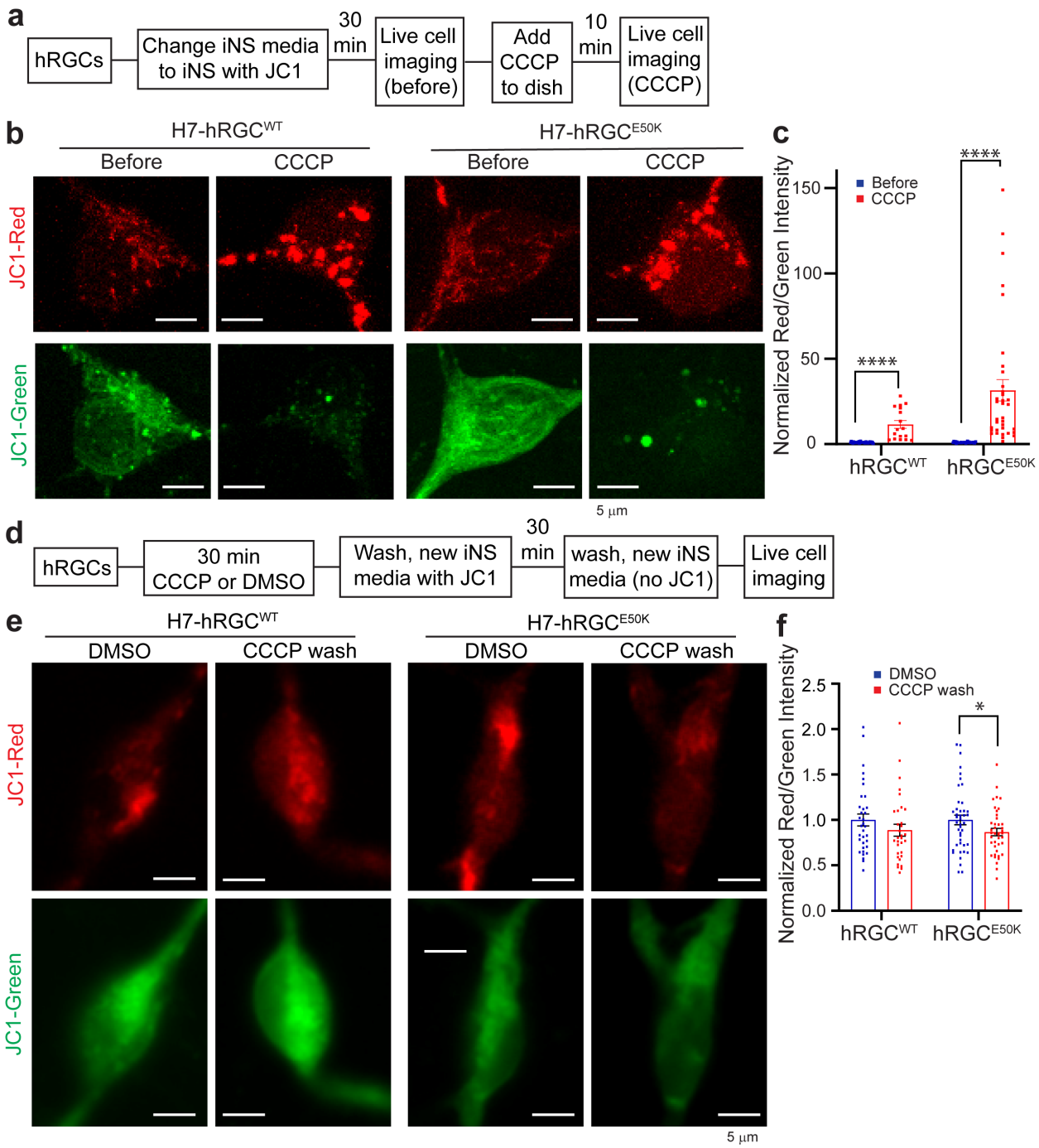

Figure 2. Under acute damage hRGCs possess efficient mitochondrial turnover mechanisms. **(a)** Schematic of JC1 experiment to monitor mitochondrial degradation and biogenesis under CCCP stress. **(b)** Representative confocal images of JC1 labelled mitochondria in hRGCs before and after 10 min CCCP treatment. JC1 dye was added 30min before CCCP and was present during treatments. Scale bars are 5 µm. **(c)** Quantification of the red-to-green fluorescence intensity ratios from the sum projections of confocal z-stacks, normalized to the corresponding before treatment values. n = 17-42 hRGCs. **(d)** Schematic of JC1 experimental design to study restoration of

mitochondrial homeostasis after CCCP washout. **(e)** Representative confocal images of JC1 labelled mitochondria in hRGCs treated with DMSO or CCCP for 30 minutes, washed, labelled with JC1 dye, washed again, and then imaged without JC1 dye present. **(f)** Quantification of the red-to-green fluorescence intensity ratios from sum projections, normalized to respective DMSO control. n=32-43 hRGCs. ∗ p-value < 0.05, ∗∗ p-value < 0.01, ∗∗∗∗ p-value < 0.0001. Unpaired student's *t-test* between independent datasets. Error bars are SEM.

Figure 3

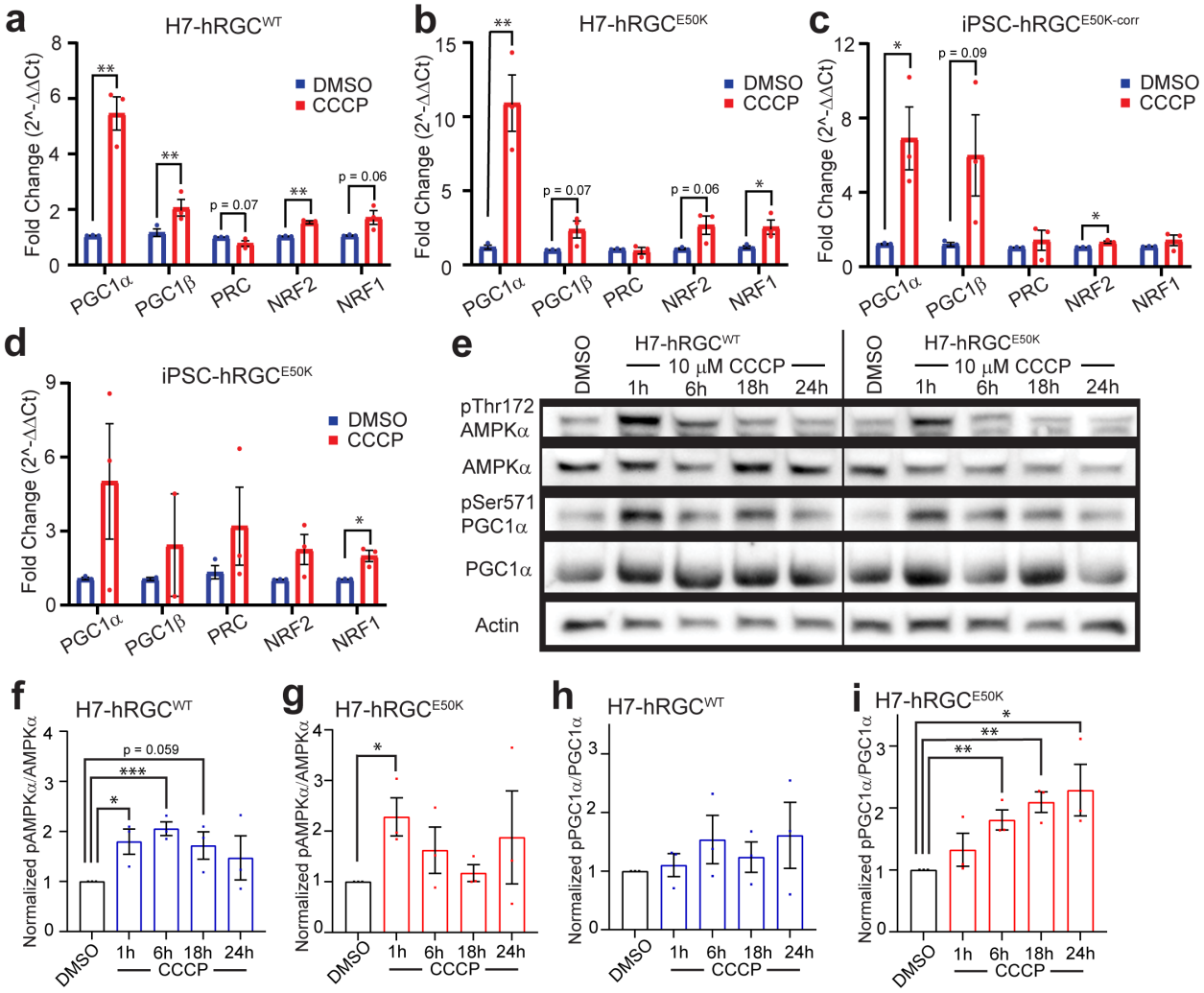

Figure 3. Mitochondrial damage activates AMPKα-PGC1α biogenesis axis in hRGCs. Mitochondrial biogenesis gene expressions in **(a)** H7-hRGC^{WT}, **(b)** H7-hRGC^{E50K} **(c)** iPSC-hRGC$^{E50K\text{-}corr}$, and **(d)** iPSC-hRGC^{E50K} derived hRGCs after 24h CCCP (10 μM) treatment. ΔΔCt fold changes were measured relative to GAPDH, and then DMSO. Error bars are SEM. n=3, 3 technical repeats averaged for each biological repeat. **(e)** Representative western blot images of H7-hRGCs treated with 10 μM CCCP for the indicated timepoints. **(f-i)** For each protein, quantification of band intensities relative to actin, then normalized to the corresponding DMSO control, **(f, g)** ratio between p-AMPKα^{Thr172} to AMPKα, and **(h, i)** ratio between p-PGC1α^{Ser571} to PGC1$^{\alpha}$. n=3. Unpaired student's *t-test* between DMSO and the individual CCCP timepoints. * p-value < 0.05, ** p-value < 0.01, *** p-value < 0.001.

Figure 4

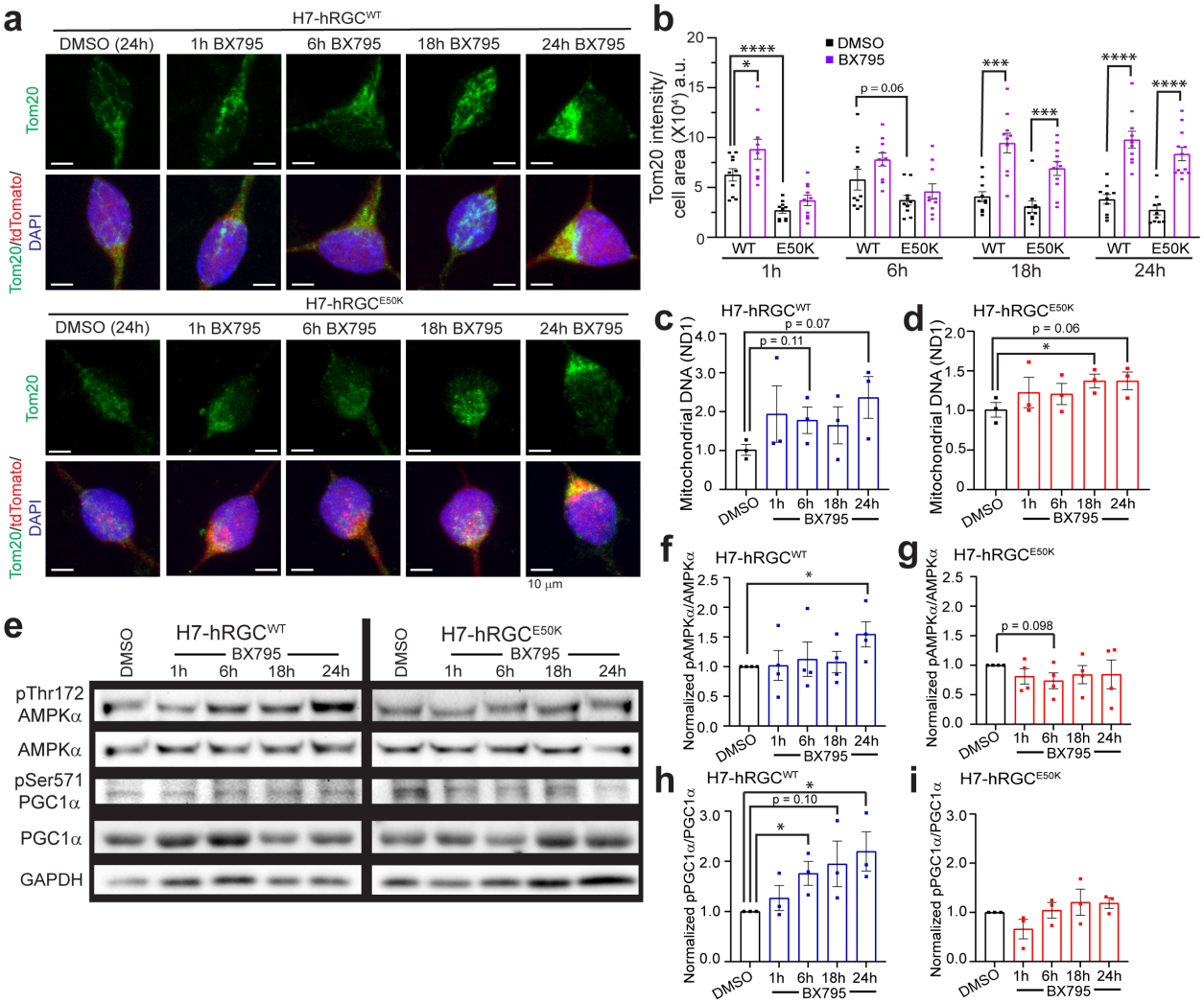

Figure 4. TBK1 inhibition activates mitochondrial biogenesis in hRGCs. (a) Representative confocal immunofluorescence images of mitochondria (Tom20) and DAPI after 1 µg/ml BX795 or equivalent DMSO treatment for the indicated time. Scale bars are 10 µm. **(b)** Quantification of Tom20 intensity per cell area from the sum projections of confocal z-stacks. n=10 cells per condition. **(c, d)** Mitochondrial DNA copy number analyzed by qPCR for mitochondrial ND1 gene normalized to nuclear RNase P gene. Results shown as ΔΔCt fold change normalized to DMSO control for different times points of 1 µg/ml BX795 treatment. n=3, 3 technical repeats averaged for each biological repeat. **(e)** Representative western blot images of H7-hRGCs treated with 1 µg/ml BX795 for indicated timepoints. **(f-i)** For each protein, quantification of band intensities relative to GAPDH, then normalized to the corresponding DMSO control, **(f, g)** ratio between p-AMPKα^{Thr172} to AMPKα, and **(h, i)** ratio between p-PGC1α^{Ser571} to PGC1α. n=3-4. * p-value < 0.05, ** p-value < 0.01, *** p-value < 0.001, **** p-value < 0.0001. Unpaired student's *t-test* between DMSO and the individual BX timepoints. Error bars are SEM.

Figure 5

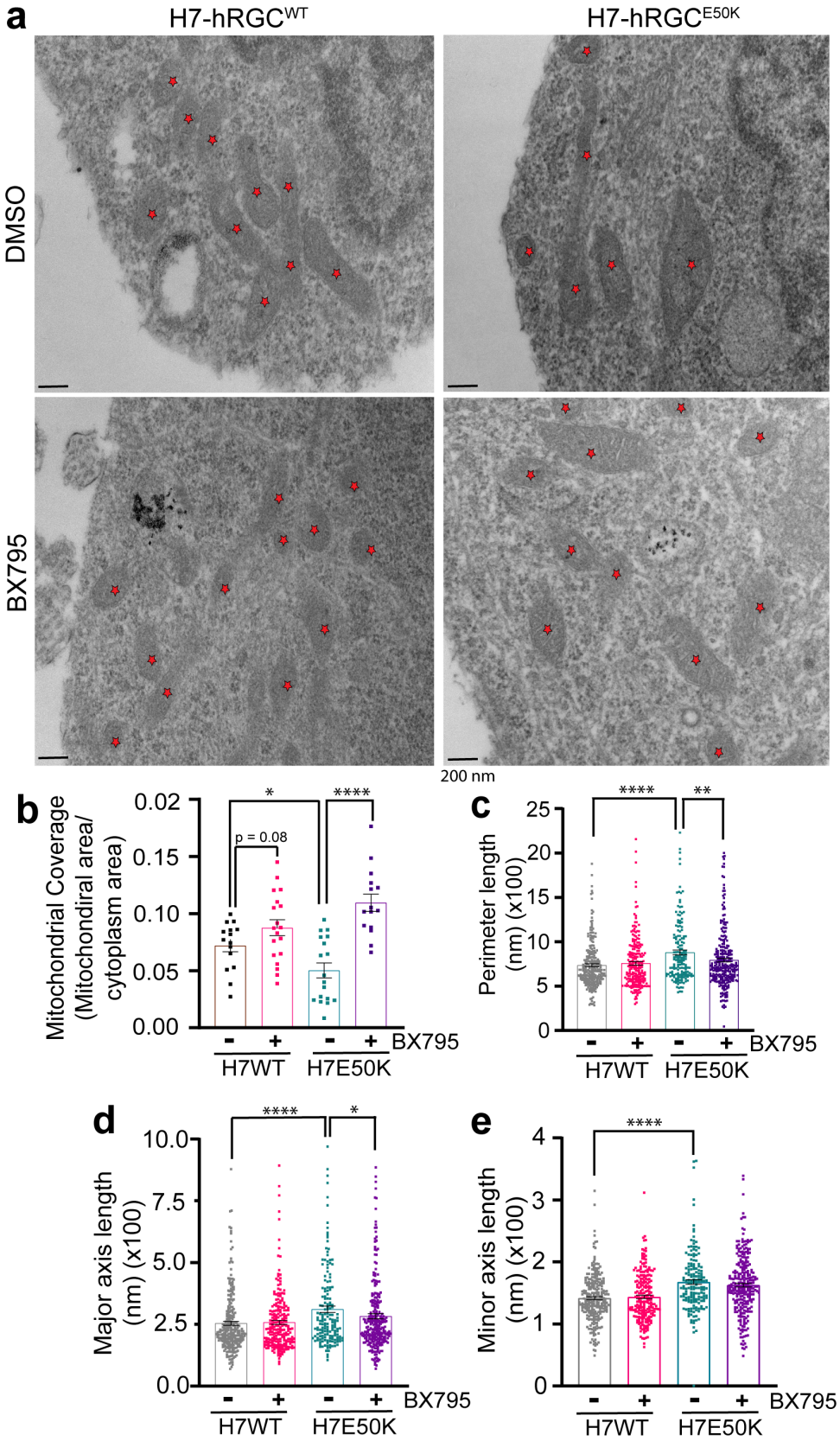
a
H7-hRGC^WT
H7-hRGC^E50K
DMSO
BX795
200 nm
b
Mitochondrial Coverage (Mitochondiral area/ cytoplasm area)
0.02
0.15
0.10
0.05
0.00
*
****
p = 0.08
- + - + BX795
H7WT H7E50K
c
Perimeter length (nm) (x100)
25
20
15
10
5
0
****
**
- + - + BX795
H7WT H7E50K
d
Major axis length (nm) (x100)
10.0
7.5
5.0
2.5
0.0
****
*
- + - + BX795
H7WT H7E50K
e
Minor axis length (nm) (x100)
4
3
2
1
0
****
- + - + BX795
H7WT H7E50K

Figure 5. TBK1 inhibition improves mitochondrial coverage and mitigates swelling in E50K hRGCs. (a) TEM images of H7-hRGC^{WT} and H7-hRGC^{E50K} after 24h DMSO or BX795 treatment, at 49000X magnification. Asterisk represents mitochondria. Scale bar = 200nm. Quantification of **(b)** mitochondrial coverage (mitochondrial area/cytoplasm area), **(c)** perimeter length, **(d)** major axis length, and **(e)** minor axis length. Unpaired student's *t-test* **(b)** or Mann Whitney U test **(c-e)** between independent datasets, * p-value <0.05, ** p-value <0.01, **** p-value <0.0001, n=15-24.

Figure 6

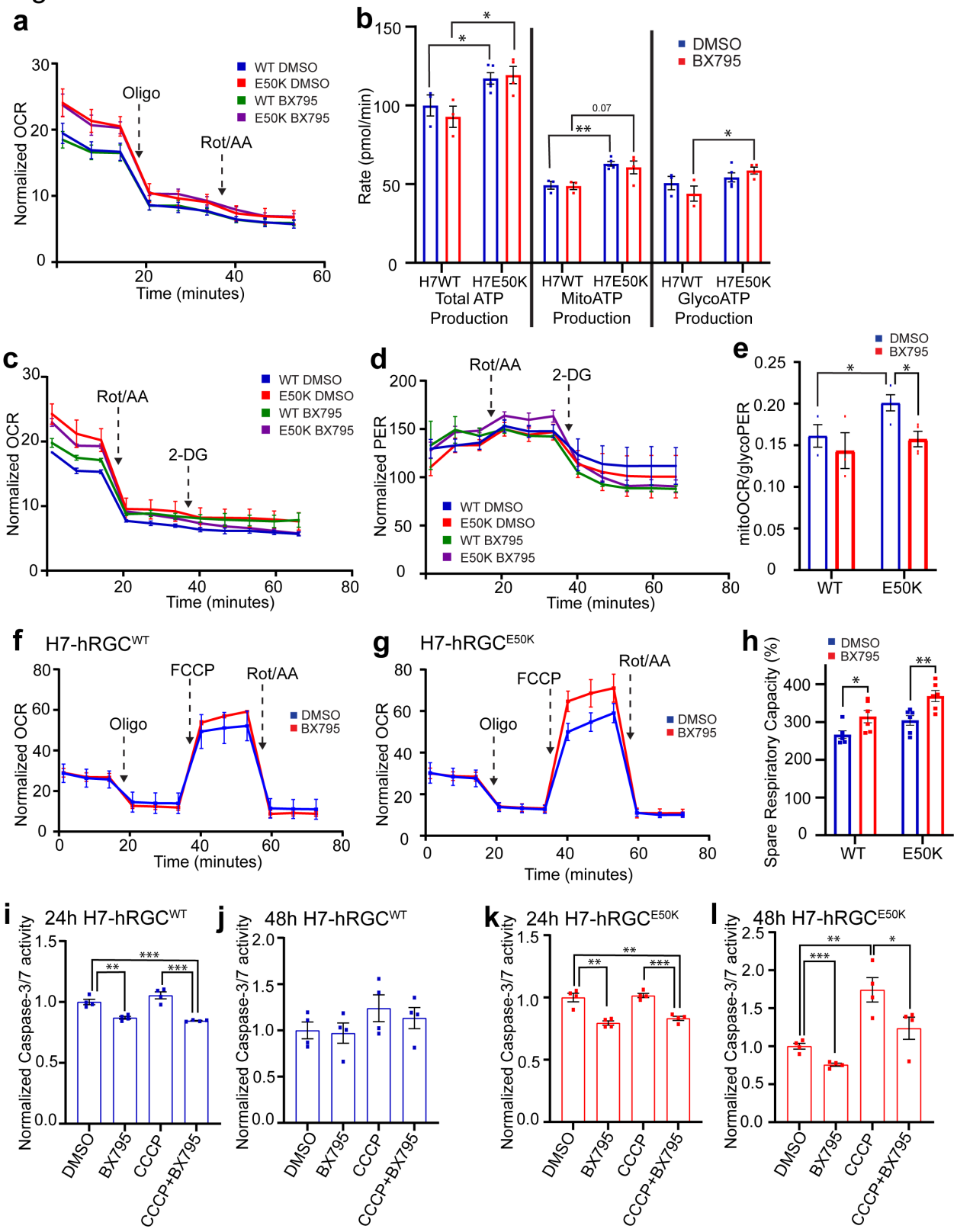
a
Normalized OCR
Time (minutes)
Oligo
Rot/AA
WT DMSO
E50K DMSO
WT BX795
E50K BX795
b
Rate (pmol/min)
DMSO
BX795
H7WT
H7E50K
Total ATP Production
MitoATP Production
GlycoATP Production
0.07
c
Rot/AA
2-DG
d
Normalized PER
e
mitoOCR/glycoPER
WT
E50K
f
H7-hRGC^WT
FCCP
g
H7-hRGC^E50K
h
Spare Respiratory Capacity (%)
i
24h H7-hRGC^WT
Normalized Caspase-3/7 activity
DMSO
BX795
CCCP
CCCP+BX795
j
48h H7-hRGC^WT
k
24h H7-hRGC^E50K
l
48h H7-hRGC^E50K

Figure 6. BX795 mediated TBK1 inhibition restores energy homeostasis and neuroprotection in glaucomatous hRGCs. (a) Measurements of cell area normalized OCR from the ATP rate assay of hRGCs treated with DMSO or 1 µg/ml BX795 for 24h. **(b)** Calculated total-, mito-, and glyco-ATP production rates from the ATP rate assay. n=3. **(c, d)** Measurements of cell area normalized **(c)** OCR and **(d)** PER from the glycolytic rate assay. **(e)** Calculated mitoOCR/glycoPER from the glycolytic rate assay. n=3 **(f, g)** Measurements of cell area normalized OCR from the Mito Stress Test of **(f)** H7-hRGC^{WT} and **(g)** H7-hRGC^{E50K}**,** and **(h)** spare respiratory capacity after 24h treatment with 1µg/ml BX795. n=6. **(i-l)** Caspase-3/7 activity was measured using ApoToxGlo-Triplex assay kit in hRGCs after 16h pretreatment with BX795 and then 24h or 48h treatment with DMSO, 1 µg/ml BX, 10 µM CCCP, or BX795 and CCCP treatments. Treatment conditions were normalized to the DMSO control for respective hRGC type. ∗ p-value < 0.05, ∗∗ p-value < 0.01, ∗∗∗ p-value < 0.001. Unpaired student's *t-test* between independent datasets.